Asphalt Internal Structure Characterization with X-Ray Computed Tomography and Digital Image Processing

Ibrahim Onifade, Denis Jelagin, Alvaro Guarin, Bjorn Birgisson, and Nicole Kringos

Department of Transport Science (TSC)
Division of Highway and Railway Engineering
KTH Royal Institute of Technology
Brinellvägen 23, SE-100 44 Stockholm, Sweden
onifade@kth.se

Abstract. In this paper, detailed study is carried out to develop a new workflow from image acquisition to numerical simulation for the asphalt concrete micro-structures. High resolution computed tomography scanned images are acquired and the image quality is improved using digital image processing techniques. Non-uniform illumination is corrected by applying an illumination profile to correct the background and flat-fields in the image. Distance map based watershed segmentation are used to segment the phases and separate the aggregates. Quantitative analysis of the micro-structure is used to determine the phase volumetric relationship and aggregates characteristics. The result of the quantitative analysis showed a very high level of reliability. Finite Element simulations were carried out with the developed micro-mechanical meshes to capture the strength and deformation mechanisms of the asphalt concrete micro-structure. From the micro-mechanical investigation the load transfer chains, higher strength characteristics and high stress localization at the mastic interface between adjacent aggregates was shown.

Keywords: X-ray computed tomography, digital image processing, finite element method, image based modeling.

1 Introduction

Asphalt concrete (AC) is a heterogeneous material which consists of mastic (binder and fines), aggregates and air-voids. The distribution of the air-voids in the matrix, the interaction between the aggregates and the mastic, and the properties of the aggregates and the mastic plays a vital role in determining the mechanical behavior of the asphalt concrete. Mainly, the aggregate properties determine the strength characteristics, the mastic determines the durability characteristics and the air-void is related to the rate of moisture damage and rutting in the asphalt concrete. The behaviour or response of the AC is highly dependent on the temperature and rate of loading. At low temperatures, it exhibits the characteristics of an elastic material

N. Kringos et al. (Eds.): *Multi-Scale Model. & Charact. of Infrastruct. Mater.,* RILEM 8, pp. 139–158.
DOI: 10.1007/978-94-007-6878-9_11

while at high temperatures above the glass transition temperature, the response is viscoelastic.

The micro-structure of AC is very complicated and it is defined by the gradation of aggregates, the orientation and number of contacts of aggregate particles, the properties of aggregate-binder interface, the voids structure, the chemical constituent of the bitumen, the texture of the stones, the adhesion between aggregates and mastic among others. [Wang, 2010]. Understanding the complex mechanical interaction that exists between the constituents of the asphalt concrete requires a reliable way to characterize the AC micro-structure.

In this context, mastic is referred to as the mixture of binder and fines. The main content of the binder is bitumen which is obtained from the fractional distillation of crude oil. The bitumen is made up of complex chains of hydrocarbon which makes it difficult to model the material using it's true chemical constituent. The hydrocarbon chains are very sensitive to changes in the environment (temperature), the rate of application of external forces or loads can also lead to a possible rearrangement of the chemical structure of the material. To overcome this difficulties, the mastic is usually represented using springs and dashpots to model the rate dependent response of the material. The Prony series, which is made up of springs and dashpots connected in series is used to model the mastic behavior in this study. In this study, the aggregates are considered as a linear elastic material and, as such, the parameters required for modeling the aggregates behavior are the Young's Modulus, the Poisson's ratio and the density.

Under loading condition, there may exist a rearrangement of the internal structure of the asphalt concrete mixture depending on the magnitude and duration of loading. The most important aspects to consider in the modeling are the contact between adjacent aggregates and the interface between the aggregate and the surrounding mastic. The morphological properties (shape, angularity and texture) determines the load transfer between aggregate particles at contact and the bonding at the interface between the mastic and aggregate particles. These properties are captured using the X-ray CT and quantified using an image processing software (Avizo).

In the past, the micro-structure of the AC has been simplified or over-idealized. Bazant et al. [Z.P. et al., 1990] and Schlangen and van Mier [Schlangen and van Mier, 1992] have represented the aggregates as rigid spherical particles while others Wittmann et al. [Wittmann et al., 1985] and Wang et al. [Wang et al., 1999] have used algorithm to generate a random micro-structure image of the asphalt concrete micro-structure. Most of these past investigations were based on 2D analyses of the asphalt concrete micro-stucture due to the complexities in generating or accurately representing the 3D micro-structure of asphalt concrete.

New techniques show a possible way to capture the micro-structure of the AC to generate models for numerical simulation, one of which is X-Ray Computed Tomography (CT). There has been a number of recent attempts to use X-Ray CT to investigate the internal structure of AC and to investigate its impact on the AC mechanical properties. Coleri et al. [Coleri et al., 2012b] used the X-ray CT to study the changes in AC micro-structure using full-scale test sections and Heavy Vehicle Simulator (HVS) loading, and X-ray CT images taken before and after HVS testing.

Coleri et al. [Coleri et al., 2012a] also used the X-ray computed tomography (CT) and digital image processing to generate the internal micro-structure of the asphalt mixtures and study the effectiveness of 2D and 3D models for the simulation of the shear frequency sweep at constant height (FSCH) test. Zelelew [Zelelew and Papagiannakis, 2011] used automated digital image processing (DIP) algorithm called Volumetrics based Global Minima (VGM) thresholding algorithm for processing asphalt concrete (AC) X-ray computed tomography (CT) images. The thresholding algorithm utilizes known volumetric properties of AC mixtures as the main criterion for establishing the air-mastic and mastic-aggregate gray scale boundary thresholds. Bhasin et al. [Bhasin, 2011] used X-ray CT images to study the 3-dimensional distribution of the mastic in asphalt composites. You et al. [You et al., 2012] developed a three-dimensional (3D) micro-structure-based computational model to predict the thermo-mechanical response of the asphalt concrete using a coupled thermo-viscoelastic, thermo-viscoplastic, and thermo-viscodamage constitutive model. You et al. [You et al., 2008] studied the dynamic modulus from the stress-strain response under compressive loads for two-dimensional 2D and three-dimensional 3D micro-structure-based discrete element models of asphalt mixtures. Masad et al. [Masad et al., 2005] developed an approach for constitutive modeling of the viscoplastic behavior of asphalt mixes and measured the micro-structure damage with X-ray computed tomography and image analysis techniques. However, very limited amount of work has been done so far for 3D image-based modeling of AC while some studies only considered the distribution of the aggregates and the mastic phase [You et al., 2012]

The air-voids, mastic and aggregates phase are considered in this study. The interface between the mastic phase and the aggregate phase is challenging to model when considering the mechanics of the mastic phase which is highly anisotropic. Further research is required to adequately understand the interaction at the boundary between the mastic and the aggregates. However, the spatial location of the contact points between adjacent aggregates is determined in this study and referred to as the contact geometry.

2 Objectives and Scope

The present study is aimed at developing the workflow from image acquisition to simulation for accurate characterization of the AC micro-structure. The main objectives of this study are to develop procedures for: (1) Segmentation of the three different phases in AC and determination of their volumetric relationship. (2) Determination of air-voids phase distribution with depth. (3) Determination of aggregates particle size gradation and distribution. (4) Determination of the distribution of contact zones between aggregates. (5) Micromechanical simulation using finite elements method (FEM).

The steps involved in this study are summarized in Figure 1

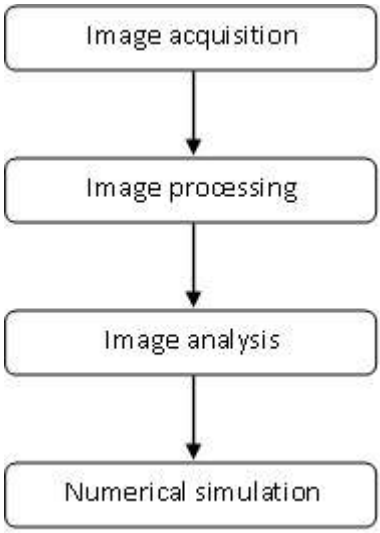

Fig. 1 Process workflow

3 Experimental Data and Scanning Procedure

In this study, the KTH X5000 CT X-ray scanner is used to obtain the detailed microscopic structure of the porous asphalt concrete core sample for further visualization, characterization and analysis. The X5000 CT scanner is a seven-axis universal x-ray imaging system designed for the inspection of large objects. It can accommodate a variety of part shapes, sizes and weights. It can produce X-ray intensities of up to 450kV.

The asphalt concrete core sample with a diameter of 100mm and a height of 80mm as shown in Figure 2 is scanned. The sample is scanned at an energy intensity of 225kV without beam filtration. The scanning resolution is 1949 x 1799 with a slice thickness of 59microns and a total of 1932 slices.

The x-ray scanning process includes sample preparation, warming-up the scanner, pre-scan settings, scanning, detector calibration and CT calibration. Beam hardening artifact is manifested in CT images with brighter edges than the center of the image. Beam hardening artifact reduces the quality of the scanned image and hence affects the phase segmentation results.

There are a number of possible techniques to reduce the beam hardening in the scanned image which includes the use of X-ray beam that is energetic enough to ensure that beam hardening is negligible, use of filters, increased exposure time among others [Ketcham and Carlson, 2001]. In this study, the beam hardening artifact is corrected using the background and flat field correction feature in Avizo Fire. The flat field is computed using the *bkgimg* command in Avizo which computes a background image from a gray level image and a binary mask (or no mask for all pixels of the image) using second order polynomial. The intensities of the 3D input image are then scaled according to the normalized intensities of the flatfield images.

Fig. 2 Porous asphalt concrete sample used in the present study

The input image gets brighter at pixels where the flatfield is dark and vice versa. In this way non-uniform illumination is compensated for [Avizo, 2009]. Other digital image processing and analysis is also performed using Avizo Fire application.

4 Digital Image Processing (DIP)

Image processing mainly involves editing and enhancement of digital image with the aim of improving the quality of the image or to extract relevant information. DIP is also used for the identification and segmentation of the different phases in the AC micro-structure.

The different techniques used in improving the quality of the acquired image include contrast enhancement, illumination correction and filtering to reduce noise in the image. Avizo background and flat field correction tool is used to correct non-uniform illumination in the acquired CT image. Non-uniform illumination correction helps to achieve improved segmentation results especially when the threshold based segmentation is used.

Filters are mainly used to reduce noise and thereby improve image quality. Different types of filters are used in image processing depending on the expected result or outcome. It is important to note that the nature of the mastic makes the segmentation process of the asphalt concrete sample a little cumbersome. Considering the fact that the mastic is a mixture of bitumen and fines, the threshold based segmentation becomes difficult as part of the mastic is identified as aggregates. This is as a result of the CT attenuation of the constituents materials in the asphalt concrete mix. Image filtering can be used to overcome this problem and thus improve the image segmentation results. Non-local means filter is used in this study to reduce the noise in the image and help improve segmentation as it smoothens regions inside objects while preventing smoothening near the edges.

Segmentation is the process of separating pixels with the same gray level value from those pixels with a different value. This is a very important step in AC image

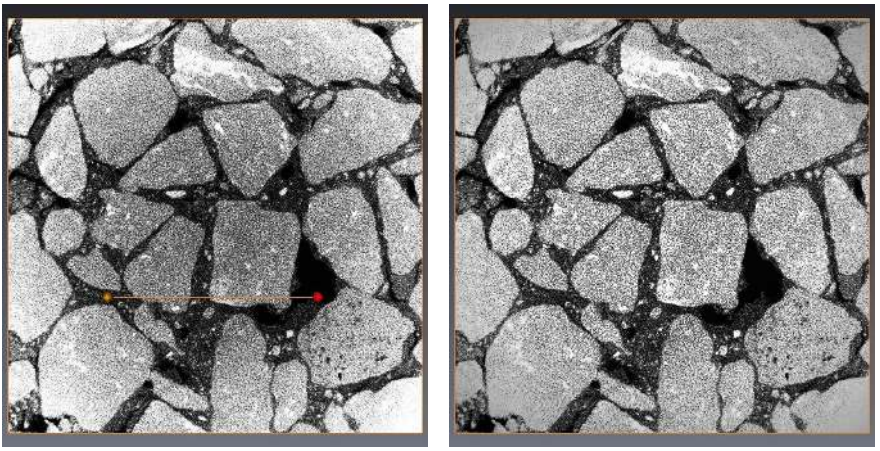

Fig. 3 a). Acquired image with beam hardening present b). Beam hardening corrected image of Asphalt concrete

processing as it is used to separate the constituents of the AC mixture. A good image resolution and contrast between the gray levels is essential for a good segmentation result. Figure 4(a) is the magnitude of the gradient showing the weak and strong edges in the image and Figure 4(b) is the plot of the grayscale along the probe line. The weak edges are variations in density in the same phase while the strong edges represent transition between adjacent phases. The magnitude of the gradient is obtained from the first derivate of the grayscale value in the x and y directions. The equations for calculation of the gradients and the magnitude are shown in equations 1 to 4.

$$(\nabla f) = [G_x^2 + G_y^2]^{\frac{1}{2}} \tag{1}$$

$$\overrightarrow{(\nabla f)} = \alpha(x,y) = tan^{-1}(\frac{G_x}{G_y}) \tag{2}$$

where

$$\frac{\partial f}{\partial x} = G_x = \frac{1}{2}(f(x+1,y) - f(x-1,y)) \tag{3}$$

$$\frac{\partial f}{\partial y} = G_y = \frac{1}{2}(f(x,y+1) - f(x,y-1)) \tag{4}$$

In 3D, one of the major challenge in processing and modeling of the AC micro-structure is the separation of the individual aggregates. Improperly separated aggregates can be seen as one big interconnected mass of stone and quantitative analysis of this interconnected stones does not give any meaningful result. Performing numerical analysis with such improperly segmented 3D micro-structure image does not simulate the behavior of the 3D mix under loading conditions. The 3D model

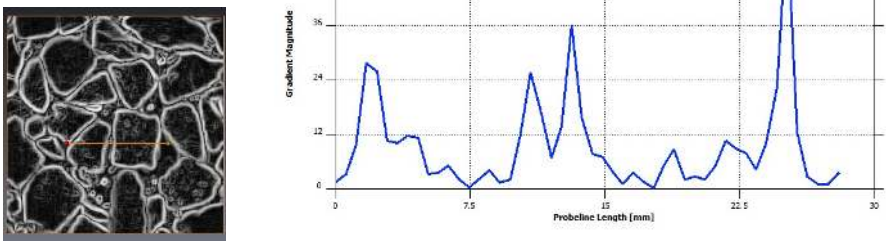

(a) (b)

Fig. 4 a). Gradient of the magnitude result showing edge of objects in the image b). Variation of gradient magnitude along probe line

Fig. 5 Phase segmented image

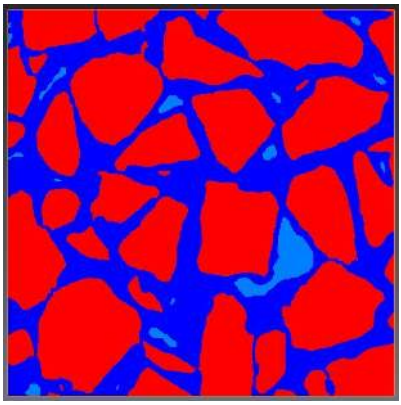

becomes too stiff and rarely deform under normal load conditions. Hence, the interaction between the aggregate and the binder is not well captured and accounted for.

To overcome this problem, different methods were employed for segmentation of the AC micro-structure. The distance-map based watershed segmentation technique gave the most satisfactory result. This method separates the aggregates in the 3D image, determines the contact point between aggregates and also create a region for mastic phase between the interface of two adjacent aggregates.

In this study, the air-void phase is segmented using basic thresholding operation since the gray intensity levels for the air-voids are quite distinct from those of the mastic and aggregates. The aggregate phase is segmented and separated using the distance-map and watershed segmentation and the mastic phase is obtained by subtracting the air-void phase and the aggregate phase from the full mask of the scanned sample. Figure 5 shows the phase-segmented AC image.

5 Digital Image Analysis and Results

After phase segmentation of the AC sample, image analysis is carried out so as to extract pertinent quantitative information. In this study, the interactive measure features of Avizo fire is used for the image analysis. The results of interest from the individual analysis of the aggregates are the Volume in 3D, Area in 3D, Feret diameter (length and width in 3D), and orientation of the aggregates. A sub-volume of $60mm \times 60mm \times 40mm$ was analyzed and the results presented in this section. For accurate aggregates size analysis, the bounding box dimensions can be used for aggregate characterization.

The volume in 3D of an object X is defined by the relationship in Equation 5 for a continuous case but estimated using Equation 6 for a discrete case. The volume is the number of pixels in region X multiplied by the volume of a voxel.

$$V(X) = \int_{R^3} (I(x,y,z)\, dxdydz) \tag{5}$$

$$V(X) = \sum_{i,j,k} I(x_i, y_j, z_k) \tag{6}$$

where
$I(x_i, y_j, z_k)$ = the intensity of the pixel of coordinates x_i, y_j, z_k
$I(x_i, y_j, z_k) = 1$ if the pixel lies within the object X and 0 otherwise

In order simplify the AC micro-structure, aggregate particles with length less than 2.34mm are considered as part of the mastic. The total number of aggregates in the sample after the clean-up is 403 stones. The distribution of the length of the stones is shown in Figure 6 and the distribution of the width in Figure 7. The 3D volume distribution of the stones is shown in Figure 8.

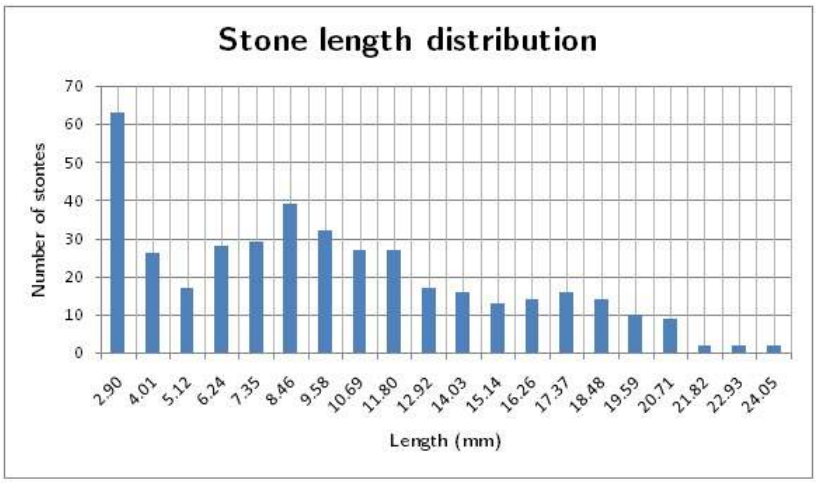

Fig. 6 Distribution of length of stones in the sample

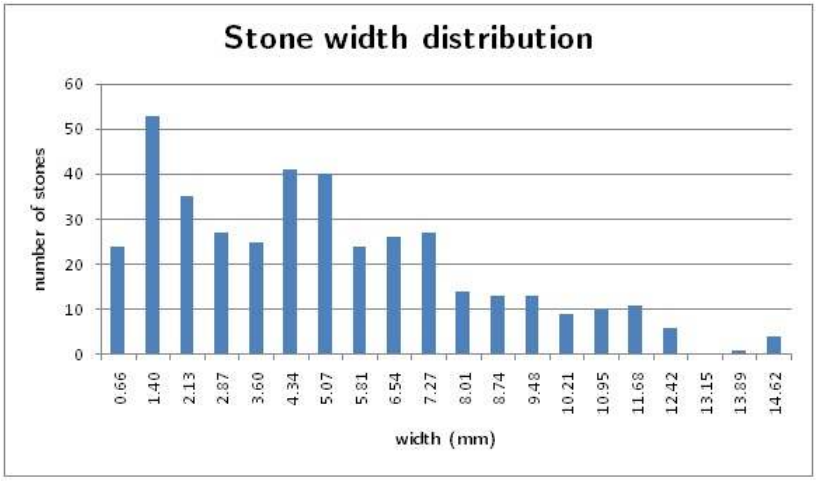

Fig. 7 Distribution of width of stones in the sample

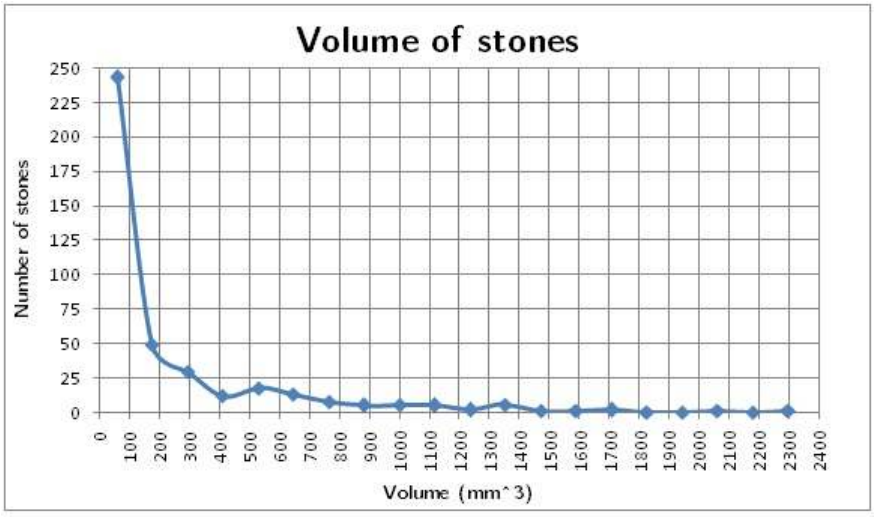

Fig. 8 Volume distribution of stones

Table 1 shows the result of the volumetric analysis of the AC sample. The result shows that the total volume of aggregates in the analyzed sample is 91109mm^2, the total volume of mastic is 36373mm^2 and the total volume of air-voids is 16468mm^2. The percentage volume of the aggregates, mastic and air-voids in the analyzed sample are 63.3%, 25.3% and 11.4% respectively. Table 2 shows the statistical relationship for the area, volume, length and width of the aggregates. Statistical relationship can be used to correlate the AC mix behaviour with geometric properties of the

Table 1 Phase Volumetric relationship

Volume	mm^3	% volume
Aggregates	91109	63.3
Mastic	36373	25.3
Air-voids	16468	11.4
Total volume of sample	143951	100

Table 2 Statistical analysis for aggregates

	$Area3d(mm^2)$	$Volume3d(mm^3)$	$Length3d(mm)$	$Width3d(mm)$
Min	1.74	0.08	2.34	0.30
Max	1221.86	2355.04	24.60	14.99
Mean	215.41	226.08	9.72	5.05
StdDev	235.10	354.75	5.37	3.26
Sum	86809.01	91109.19	3917.45	2034.24

stones. The relationship also gives relevant information that can be used to study asphalt mix design reliability and the micro-structure variability.

Distribution of the air-voids with depth is obtained by calculating the 2D area of air-voids per slice. The 2D area of air-voids is then calculated for each slice along the depth of the sample. Figure 9 shows the variation of the air-voids with sample depth. A practical application of the air-voids distribution is the assessment of compaction in AC sample. The variation of the air-voids can be used as a quality control measure to check the uniformity and adequacy of compaction effort on AC pavements. It can also be used as a tool to assess the condition of existing AC pavements.

It can also be used to examine crack initiation and propagation in AC mixtures. The distribution of the air-voids can be captured in the x, y and z coordinates before the application of mechanical load on the AC sample. After loading, the variation of the air-voids distribution can be used together with other related information to accurately determine the micro-structure evolution as a result of loading.

The contact between adjacent aggregates is captured using a combination of digital imaging techniques. The watershed lines and the aggregate mask used for the segmentation of the aggregate phase is used to determine the location of contacts between aggregates. It is interesting to find out that the air-voids distribution is inversely proportional to the contacts area distribution. It is worthy to note that the processed sample is a porous asphalt sample that have undergone aggregates segregation as a result of clogging. We have more fine particles at the top of the sample and more coarse particles at the bottom. There are more inter-particle contacts and less air-voids at the bottom of the sample. In the same sense, there are more air-voids at the top of the sample and less contacts between the fine aggregates. Figure 10 shows the contact area distribution of the sample.

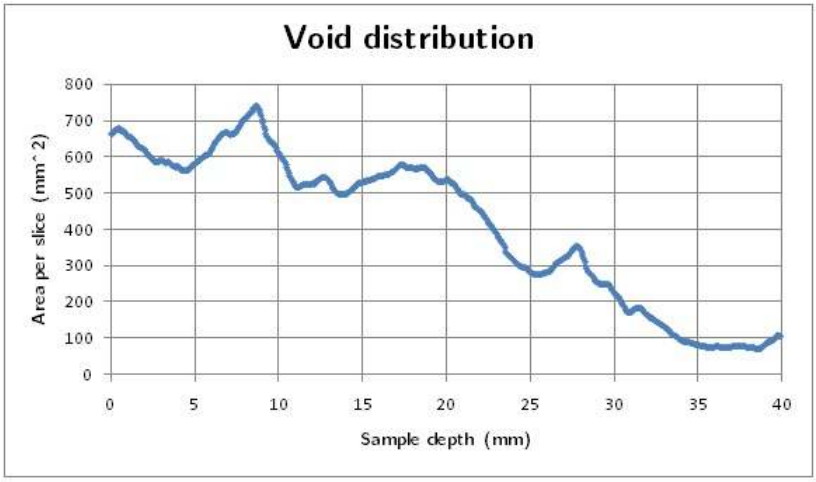

Fig. 9 Density distribution of air-voids with depth

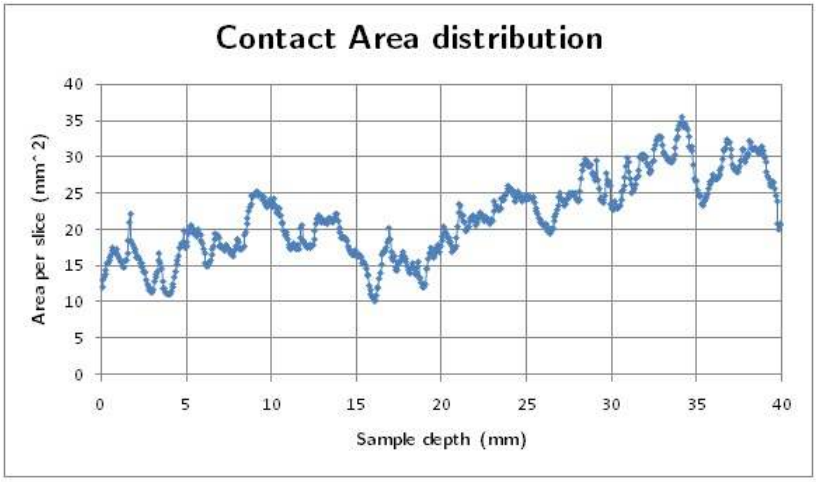

Fig. 10 Stone contact areas with depth

6 Surface and Mesh Generation

The segmented image of the AC microstructure is imported into Simpleware for surface generation and mesh construction. The air-void, mastic and aggregates phases are assigned a grey level of 1, 2 and 3 respectively for identification.

During surface generation, the sample is resampled to simplify the surface and reduce the number of elements generated during the mesh generation. Scanning at

high resolutions helps to capture the pertinent microstructure details and may be suitable for computer visualization. However, this high resolution images are not suitable for finite element analysis as it will take a lot of computer resources to process and run finite element analysis on them. The tweak is to be able to reduce the number of triangles that make up the surface without losing important geometric information.

The surface generated from the acquired image with a resolution of 59microns consists of 98Million triangles before resampling. A comparative study was carried out to determine what amount of resampling will be allowed without loosing considerable amount of details. Figure 11 shows the change in the volume of the different phases with respect to change in resampling resolution. From the study, a resampling resolution of 400micron was considered suitable. After resampling to a resolution of 400microns, the number of triangles was reduced to 12.4M which is about 12.6% of the original amount of triangles.

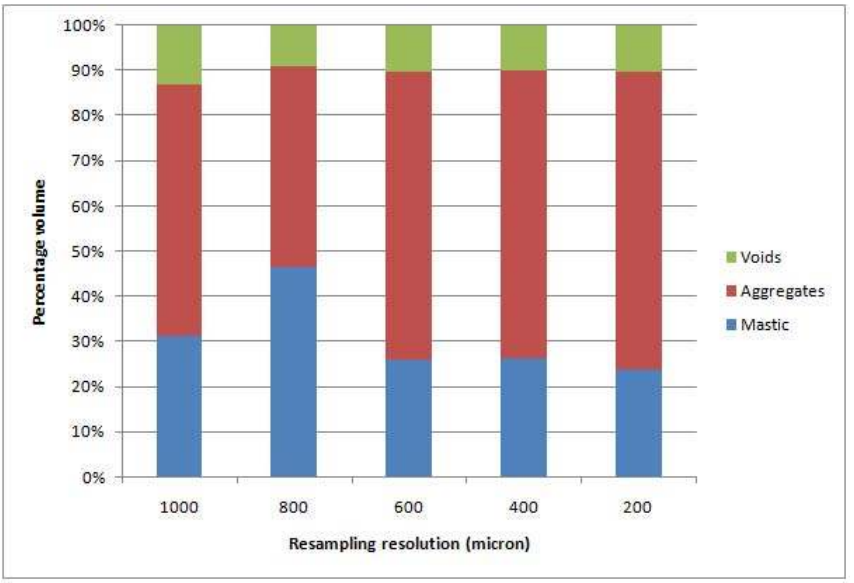

Fig. 11 Comparative study of resampling resolution

Due to limited computer power, a subsample of $30mm \times 30mm \times 30mm$ was taken for mesh generation and transfer into Finite Element (FEM) application for numerical simulation. The mesh was generated using the FE+ grid utility of simpleware. The resulting amount of tetrahedral mesh generated for the $30mm \times 30mm \times 30mm$ sub-volume is 254,000 tets. Simpleware can be used to define the interface and contact between different phases during the mesh generation. These information can be useful for further study of the aggregate-binder interaction in the AC matrix.

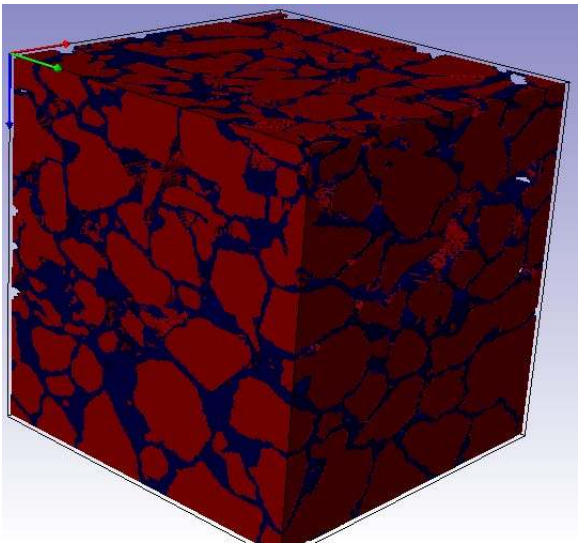

Fig. 12 Surface regeneration of 60x60x60mm AC sample

7 Micromechanical Finite Element (FE) Analysis

In this study, numerical simulation is carried out to investigate the behaviour of the AC microstructure under the action of mechanical loading. Three dimensional (3D) uniaxial compression FEM analysis was carried out on a geometry extracted from the AC microstructure, which is made up of two stones connected with mastic to show local stress and strain distributions. The same uniaxial compression analysis is then carried out on the $30mm \times 30mm \times 30mm$ meshed geometry. It was assumed that there is stress continuity at the interface between the mastic and aggregates as the mechanics of stress transfer between such interface is still under study. The numerical simulation is carried out using COMSOL Multiphysics.

7.1 Material Parameter

In this study, the aggregates is considered as a linear-elastic material while the mastic is considered as a linear-viscoelastic material. The material parameters required to model the elastic behaviour of the aggregates are the Young's modulus, Poission ratio and the density of the aggregates.

The time-dependent mastic property is considered using the Boltzmann superposition principle 7. The maxwell model in the form of a Prony series is used to model the rate dependent behavior of the mastic. The Maxwell model is represented by a series of viscous damper and elastic strings to simulate the viscous and elastic behavior respectively as shown in 13. A 5-leg/chain viscoelastic Maxwell model is used in this study. The viscoelastic model parameters required to model the mastic

behavior are the relaxation time (η_m), the relaxation modulus (E_m), the instantaneous shear modulus (G_0). The time-temperature dependence is modeled using the Williams-Landel-Ferry (WLF) shift function to obtain the shift factors(a_T) at different temperatures.

$$\sigma(t) = \int_0^t E(\xi(t) - \xi(\tau)) \frac{\partial \varepsilon(\tau)}{\partial \tau} d\tau \tag{7}$$

From equation 7, $E(\xi(t) - \xi(\tau))$ is the relaxation modulus at the reduced time $(\xi(t) - \xi(\tau))$ and the reduced time is defined by equation 8. The expression for the WLF shift function is shown in equation 9. From equation 9, T is the selected temperature, T_0 is the reference temperature, C1 and C2 are material constants.

$$\xi = \int_0^t \frac{1}{a_T} dt \tag{8}$$

$$log(a_T) = \frac{-C1 * (T - T_0)}{C2 + (T - T_0)} \tag{9}$$

The viscoelastic material parameters used to model the time-dependent behavior of the mastic was obtained from [You et al., 2012]. The material parameters were obtained from DSR test with a loading time of 1000sec and at a reference temperature of 20°C. The creep behavior has been presented as creep compliance data in [You et al., 2012]. The creep compliance data was converted into relaxation spectrum shown in Table 3 for modeling the mastic material behavior in COMSOL. The Laplace-Transform domain was used to convert the creep compliance data to stress relaxation functions using equations 10 to 12 .

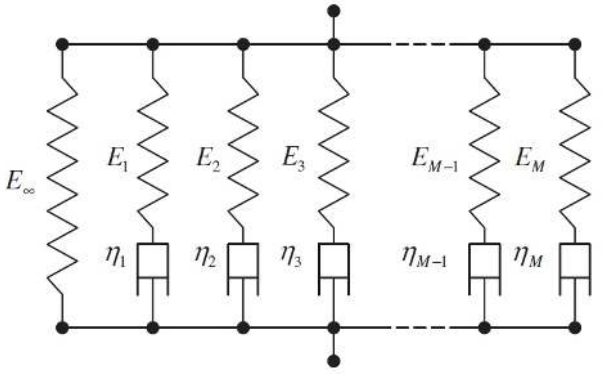

Fig. 13 Prony series

Table 3 Viscoelastic relaxation model parameters

M	$\eta_m(s)$	$E_m(MPa)$
1	0.1	20.7
2	1	46.2
3	10	52.8
4	100	53.5
5	1000	53.6

$$\tilde{G}(s)\tilde{J}(s) = 1 \tag{10}$$

where s = Laplace variable

$$\tilde{G}(s) = G_\infty + \sum_{i=1}^{n} \frac{s\rho_i G_i}{s\rho_i + 1} \tag{11}$$

$$\tilde{J}(s) = J_\infty + \sum_{k=1}^{m} \frac{\lambda_k}{s\lambda_k + 1} \tag{12}$$

7.2 Three-Dimensional (3D) Uniaxial Compression

Uniaxial compression simulation is used to investigate the stone breakage and polishing during compaction. The 3D geometry is extracted from the AC microstructure and it consists of two (2) aggregates interconnected with mastic. A uniaxial compressive displacement of 0.01mm is applied at one end of the model with the other end restrained as shown in Figure 14. The mastic is modeled as linear-viscoelastic material and the aggregates as linear elastic material. The material parameters used to model the viscoelastic behaviour of the mastic is shown in 3. The Young's modulus is selected from the work of [You et al., 2012] and considered to be 25GPa, the poisons ratio is 0.25 and the density is 4000kg/m3.

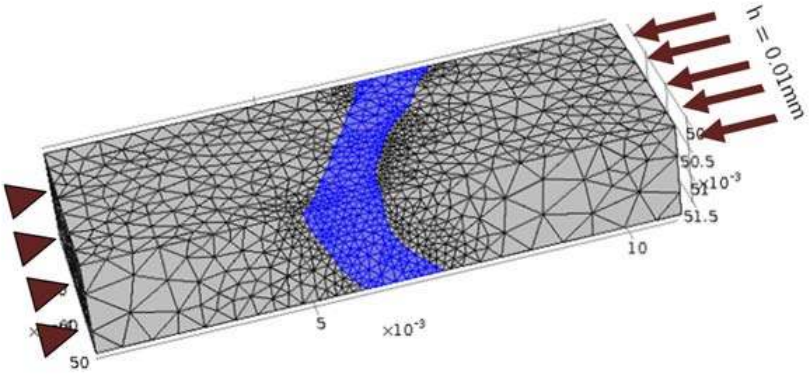

Fig. 14 3D uniaxial compression model

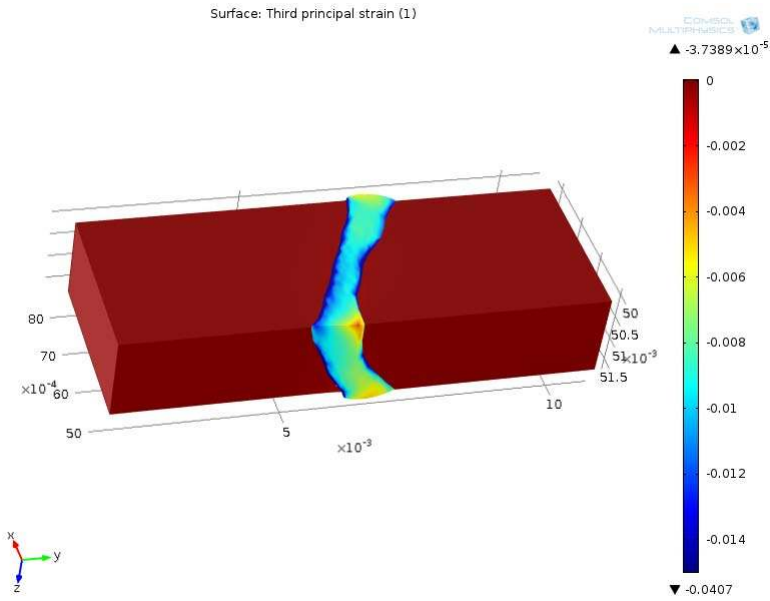

Fig. 15 Compressive strain distribution in x-direction

Figures (15) shows the strain distribution in the 3D model. It can be seen that compressive strains are localized in the binder with a maximum strain of 4.07%. High compressive strains are developed close to the aggregate-mastic interface and at regions with small mastic thickness.

Figures (16) shows the Von Mises stress distribution for the 3D model. The Von Mises stress localized in stones with high stress intensities around contact points between aggregates at aggregate-mastic interface.

Figure (17) shows the mesh for the 30mm x 30mm x 30mm AC geometry. The mesh was generated using Simpleware and contains a total of 254,000 tetrahedral elements. A time-dependent uniaxial displacement was applied at the top of the sample at a rate of 0.001mm/sec and the load displacement was applied for a 10sec period. The total displacement at the top of the sample after 10sec of analysis was 0.01mm which corresponds to the same displacement applied to the geometry in the first uniaxial compression case.

Figure (18) shows the strain distribution in the AC sample. The maximum strain localized in the mastic is 1.2%. Load transfer zones can be observed in Figure (18) which reconfirms the importance of the internal structural arrangement of the AC mix to load response. Figure (19) shows the stress distribution with high stress concentration at the edge and contact between stones.

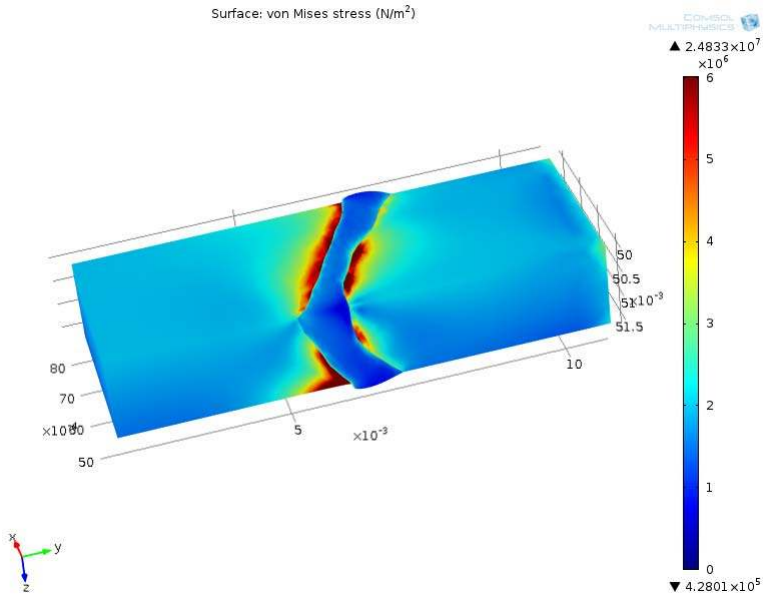

Fig. 16 Von Mises stress distribution in 3D model

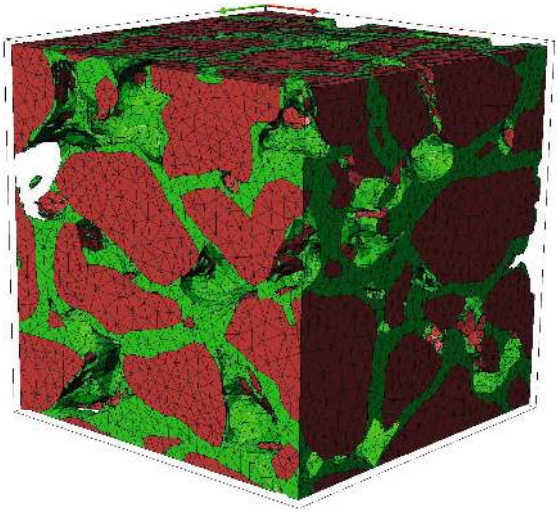

Fig. 17 Mesh of 30mm x 30mm x 30mm AC sample

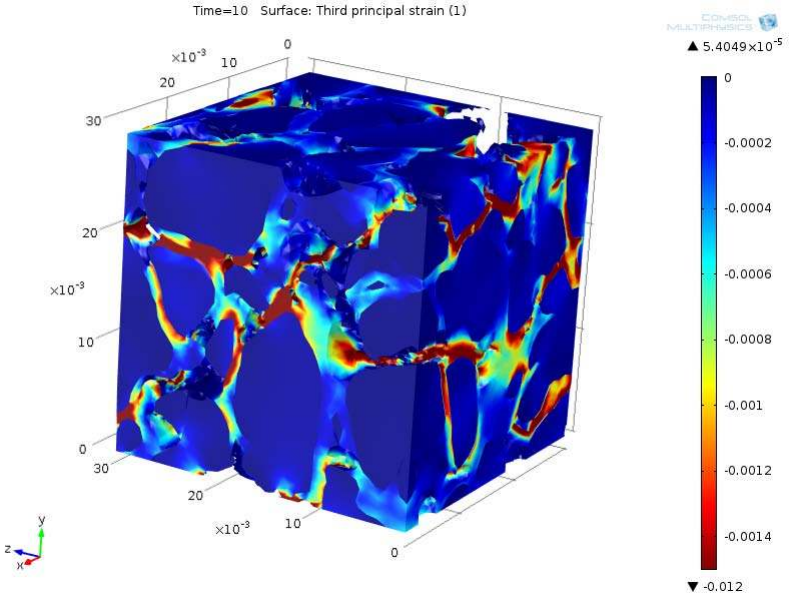

Fig. 18 Compressive strain distribution in 30mm x 30mm x 30mm model

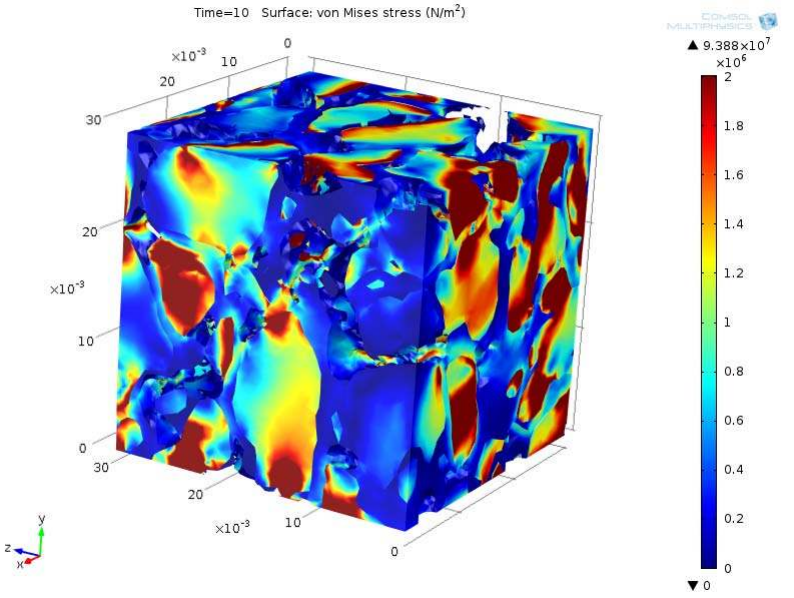

Fig. 19 Von Mises stress distribution in 30mm x 30mm x 30mm model

8 Conclusion

The present study have shown and described the workflow process from image acquisition to micro-mechanical numerical simulation using X-Ray computed tomography and digital image processing techniques. Phase segmentation of the AC micro-structure using thresholding operations does not produce good segmentation results. A non-linear filter together with the distance map based watershed segmentation is used to segment the phases in the AC micro-structure and also to separate adjacent aggregates.

Digital image analysis techniques is used to analyze the phase segmented AC micro-structure. Digital image analysis is used to determine phase volumetric relationships and individual aggregate properties like volume of aggregates, length and width of aggregates, orientation of aggregates and spatial location of aggregates in the AC mix and air-void distribution.

Numerical simulation is used to study the strength and deformation mechanisms in order to characterize the AC micro-structure using a 3D finite element analysis. Load transfer chains can be observed in the micro-structure model with strains localization in the mastic. Further study of the behavior at the aggregate-mastic interface using X-Ray computed tomography and Digital Image Processing can be used to understand the mechanism of debonding and stripping of aggregates so as to mitigate them. This can help to further improve mix performance and reduce permanent deformations in the road pavements.

References

[Avizo, 2009] Avizo: Avizo User's Guide. Visualization Sciences Group, Vordeaux (2009)

[Coleri et al., 2012a] Coleri, E., Harvey, J.T., Yang, K., Boone, J.M.: Development of a micromechanical finite element model from computed tomography images for shear modulus simulation of asphalt mixtures. Construction and Building Materials 30(0), 783–793 (2012a)

[Coleri et al., 2012b] Coleri, E., Harvey, J.T., Yang, K., Boone, J.M.: A micromechanical approach to investigate asphalt concrete rutting mechanisms. Construction and Building Materials 30, 36–49 (2012b)

[Ketcham and Carlson, 2001] Ketcham, R.A., Carlson, W.D.: Acquisition, optimization and interpretation of x-ray computed tomographic imagery: applications to the geosciences. Comput. Geosci. 27(4), 381–400 (2001)

[Masad et al., 2005] Masad, E., Tashman, L., Little, D., Zbib, H.: Viscoplastic modeling of asphalt mixes with the effects of anisotropy, damage and aggregate characteristics. Mechanics of Materials 37(12), 1242–1256 (2005)

[Schlangen and van Mier, 1992] Schlangen, E., van Mier, J.: Simple lattice model for numerical simulation of fracture of concrete materials and structures. Materials and Structures 25, 534–542 (1992)

[Wang, 2010] Wang, L.: Mechanics of Asphalt: Microstructure and Micromechanics. McGraw-Hill (2010)

[Wang et al., 1999] Wang, Z., Kwan, A., Chan, H.: Mesoscopic study of concrete i: generation of random aggregate structure and finite element mesh. Computers and Structures 70(5), 533–544 (1999)

[Wittmann et al., 1985] Wittmann, F., Roelfstra, P., Sadouki, H.: Simulation and analysis of composite structures. Materials Science and Engineering 68(2), 239–248 (1985)

[You et al., 2012] You, T., Al-Rub, R.K.A., Darabi, M.K., Masad, E.A., Little, D.N.: Three-dimensional microstructural modeling of asphalt concrete using a unified viscoelastic viscoplastic viscodamage model. Construction and Building Materials 28(1), 531–548 (2012)

[You et al., 2008] You, Z., Adhikari, S., Dai, Q.: Three-dimensional discrete element models for asphalt mixtures. Journal of Engineering Mechanics 134(12), 1053–1063 (2008)

[Zelelew and Papagiannakis, 2011] Zelelew, H.M., Papagiannakis, A.T.: A volumetrics thresholding algorithm for processing asphalt concrete x-ray ct images. International Journal of Pavement Engineering 12(6), 543–551 (2011)

[Z.P. et al., 1990] Bazant, Z.P., Tabbara, M.R., Kazemi, M.T., Pijaudier-Cabot, G.I.: Random particle model for fracture of aggregate or fiber composites. Journal of Engineering Mechanics 116, 1686–1705 (1990)